NANO LETTERS

pubs.acs.org/NanoLett Letter

Arbitrary Programming of Racetrack Resonators Using Low-Loss Phase-Change Material Sb_2Se_3

Zhuoran Fang,[#] Brian Mills,[#] Rui Chen, Jieying Zhang, Peipeng Xu, Juejun Hu,* and Arka Majumdar*

Cite This: https://doi.org/10.1021/acs.nanolett.3c03353 Read Online

ACCESS | Metrics & More | Article Recommendations | Supporting Information

ABSTRACT: The programmable photonic integrated circuit (PIC) is an enabling technology behind optical interconnects and quantum information processing. Conventionally, the programmability of PICs is driven by the thermo-optic effect, free carrier dispersion, or mechanical tuning. These effects afford either high speed or a large extinction ratio, but all require constant power or bias to maintain the states, which is undesirable for programmability with infrequent switching. Recent progress in programmable PICs based on nonvolatile phase-change materials (PCMs) offers an attractive solution to a truly "set-and-forget" switch that requires zero static energy. Here, we report an essential building block of large-scale programmable PICs—a racetrack resonator with independent control of coupling and phase. We changed the resonance extinction ratio (ER) without perturbing the resonance wavelength, leveraging a programmable unit based on a directional coupler and a low-loss PCM Sb_2Se_3. The unit is only 33-μm-long and has an operating bandwidth over 50 nm, a low insertion loss (~0.36 dB), high ER (~15 dB), and excellent fabrication yield of over 1000 cycles endurance across nine switches. The work is a crucial step toward future large-scale energy-efficient programmable PICs.

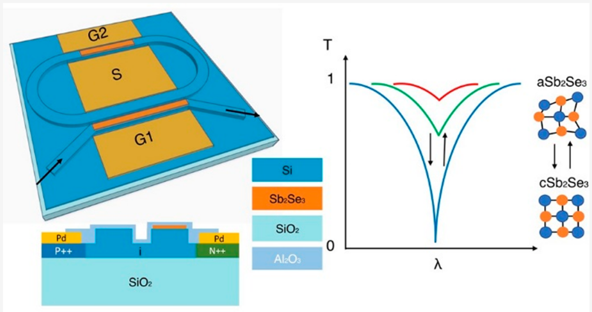

KEYWORDS: *photonic integrated circuits, optical switch, phase-change materials*

Programmability is an essential feature in modern-day integrated photonic systems and is crucial to enable technologies from next-generation data centers,[1] to optical neural networks,[2] and quantum information processing.[3] A key building block for many programmable PICs is a microring resonator whose coupling and phase can be independently controlled. Such arbitrary programming of the microring requires extremely local tuning and "set-and-forget" reconfiguration with zero static energy to hold the programmed states—a prerequisite for a truly programmable PIC. However, this is a near-impossible task for conventional programming methods such as thermo-optic effect[4] and mechanical tuning.[5] Chalcogenide-based phase-change materials (PCMs), exemplified by $Ge_2Sb_2Te_5$ (GST), present an ideal solution to the above scenarios, achieving both local and nonvolatile tuning, thanks to their nonvolatile reversible microstructural phase transition, multilevel operation, and large refractive index contrast. They can also be programmed at a relatively fast time scale (ns to μs) with moderate switching energy (pJ to nJ).[6] Despite recent progress in PCM-based programmable PICs,[7−10] simultaneously achieving a compact footprint, low loss, and operation over a broad wavelength range remains to be challenging. A recent work shows that an ultracompact phase-shifter (L_π of 11 μm) can be achieved using Sb_2Se_3,[9] but the Mach−Zehnder Interferometer (MZI) configuration is prone to phase error and has a large overall footprint (>100 μm) when the 3-dB couplers are included.[4] Another approach is to use a directional coupler configuration that does not need 3-dB couplers to split the light. However, the device footprint is still long with a coupling length (L_c) of 64 μm using $Ge_2Sb_2Te_5$ (GST)[11] and 79 μm using Sb_2S_3,[12] which is due to the trade-off between refractive index contrast (Δn) and the extinction coefficient (k). GST has a large $\Delta n \sim 3$ but also a large $k \sim 1$ near 1550 nm. To circumvent the loss of crystalline GST, a third waveguide is typically added in between the two original waveguides to allow for symmetric low-loss operation.[13,14] Since the light must couple from the top waveguide to the middle waveguide first before going into the bottom waveguide, the coupling length essentially doubles. By using low-loss PCM Sb_2S_3 ($k \sim 0$), the middle waveguide is no longer needed, but the smaller index contrast of Sb_2S_3 ($\Delta n \sim 0.5$) also results in a longer L_c to ensure no coupling to the bar state.[12]

Here, leveraging the large $\Delta n/k$ of Sb_2Se_3 ($\Delta n \sim 0.77$ and $k \sim 0$ at 1550 nm),[9] we design and experimentally demonstrate an ultracompact broadband directional coupler switch with an

Received: September 3, 2023
Revised: December 19, 2023
Accepted: December 19, 2023

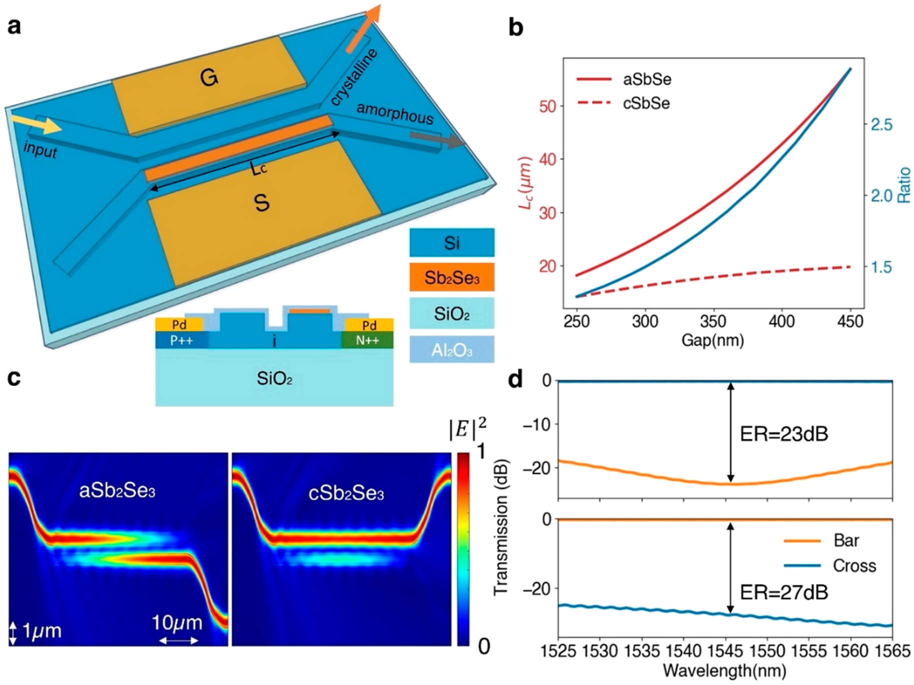

Figure 1. Design of the directional coupler switch. (a) Schematic of the directional coupler switch. Inset below shows the cross-section of the device. (b) Coupling length against the gap for aSb_2Se_3 and cSb_2Se_3-loaded hybrid waveguides. The ratio is the coupling length of aSb_2Se_3 over that of cSb_2Se_3. (c) FDTD simulated electric field intensity of the directional coupler in cross (amorphous) and bar (crystalline) states. (d) FDTD simulated transmission spectra of the directional coupler in cross (top) and bar (bottom) states.

L_c of 33 μm, a 50 nm bandwidth, ∼0.36 dB insertion loss, and ∼15 dB/8 dB (bar/cross) extinction ratios. The coupling length is 50% shorter compared to that of the state-of-the art. This compact switch enables us to independently control coupling and phase inside a racetrack resonator—a demanding task for traditional thermo-optic phase shifters due to the thermal crosstalk.[15,16] The independent modulation of coupling and phase allows tuning the extinction ratio of a resonance in a nonvolatile way without shifting the resonance wavelength. Last, we show high device yield by performing endurance tests on nine directional coupler switches, all of which can be switched more than 1000 cycles while maintaining a large contrast of >10 dB. This work paves the way to large-scale programmable PICs with zero static energy.

We design the directional coupler switch such that the light couples to the cross port when the PCM is in the amorphous state and to the bar port when the PCM is in the crystalline state (Figure 1a). The switch is fabricated on a 220 nm silicon-on-insulator (SOI) platform and the waveguide is partially etched with a 100 nm slab to allow doping that forms a PIN microheater.[17] We sweep the coupling gap between the Si bare waveguide and the Sb_2Se_3-loaded hybrid waveguide to extract the difference between the effective indices of the even and odd supermodes (see section S1 in the Supporting Information for calculating the effective indices of the supermodes). From these effective indices, the coupling length L_c is calculated via coupled mode theory.[18] Coupling lengths for both aSb_2Se_3 and cSb_2Se_3 are plotted in Figure 1b in red lines, and the blue line indicates the ratio, i.e., L_c in the amorphous state over L_c in the crystalline state. The shortest L_c that satisfies our requirement is when the ratio equals 2.[18] This can be understood by the fact that the light couples once to the hybrid waveguide and leaves the cross port in the amorphous state. In the crystalline state, the light first couples to the hybrid waveguide, before coupling back to the bare Si waveguide, and then leaves the bar port; i.e., the coupling happens twice, see Figure 1c. The simulated transmission spectrum is shown in Figure 1d with a broad operating bandwidth over 40 nm and less than −20 dB of crosstalk in both states. The insertion loss is ∼0.35 dB (∼0.37 dB) in the amorphous (crystalline) state. There are two main sources of loss, which can be identified in Figure 1c. A breakdown of the losses is presented in Table S1 of the Supporting Information (SI). First, light is lost at the input and output S bends (∼0.2 dB per bend) due to the tight 10 μm bend radius of partially etched waveguides, see also Figure S2 in the SI. A tight waveguide bend is used to reduce the finite-difference time-domain (FDTD) simulation region so that finer mesh can be used at the coupling region. In the experiment, we switched to a 20 μm bend, which has negligible bend loss.[17] The second source of loss comes from mode mismatch between the bare Si waveguide and the hybrid waveguide, which is clearly visible in the transition region in Figure 1c. We estimate a reflection loss of ∼0.05 dB per facet, see Figure S2 in the SI. The reflection loss can be avoided in the future by tapering the PCMs. Figure S3 in the SI shows the simulation for light injecting from the lower port, which confirms that the directional coupler switch is also symmetric in optical response despite being asymmetric geometrically.

The device is fabricated by lithography and etching (see Methods). To find the optimal phase matching conditions, we first fabricated a chip with many device designs to scan a wide parameter window of hybrid waveguide width while keeping the bare Si waveguide width unchanged. To simplify the fabrication, these devices were not doped or metallized, and the phase transition is induced by rapid thermal annealing under a N_2 atmosphere. The experimental results are shown in section S8 in the SI, where we have identified two designs with <1 dB loss and a larger than 10 dB extinction ratio in both

https://doi.org/10.1021/acs.nanolett.3c03353
Nano Lett. XXXX, XXX, XXX−XXX

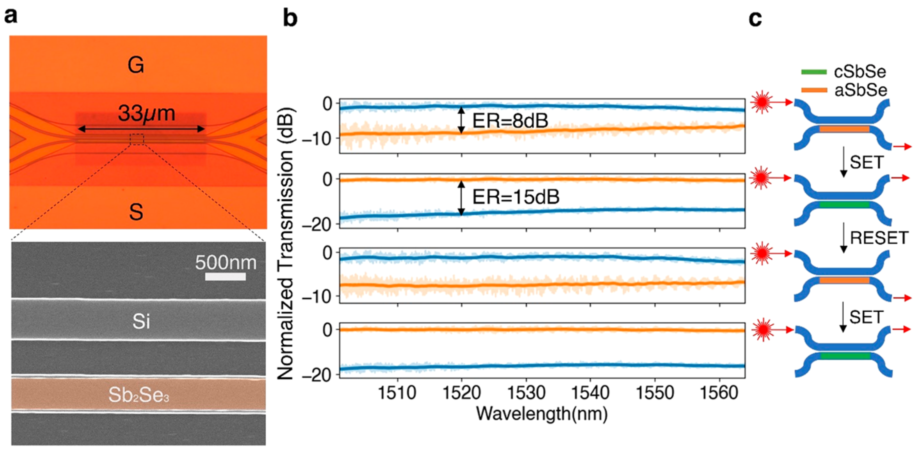

Figure 2. Electrical control of the directional coupler switch. (a) Optical micrograph (top) and SEM (bottom) of the fabricated switch. (b) Experimental transmission spectrum of the reversible switching between cross and bar states. 3.6 V, a 1.5 ms width, and a 0.5 ms trailing edge were used for SET. 8.2 V, a 400 ns width, and an 8 ns trailing edge were used for RESET. The spectrum is normalized by the spectrum of a waveguide near the device to remove the grating coupler spectrum. A Savitsky−Golay filter with a window size of 501 was applied to smooth out the spectrum. The unsmoothed data are shaded in the background. (c) Schematic showing the state of the switch, corresponding to the spectrum shown in b.

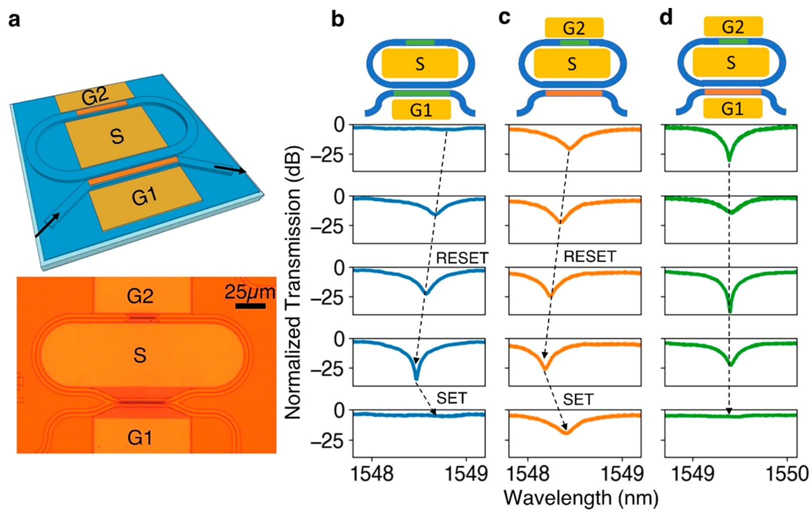

Figure 3. Arbitrary programming of a racetrack resonator. (a) Schematic (top) and the optical micrograph (bottom) of the racetrack resonator. (b) Controlling the coupling between the racetrack and the bus waveguide. For RESET, pulses of 5.6, 5.7, and 5.8 V were used with a 400 ns width and 8 ns trailing edge. For SET, a pulse of 2.6 V, a 1.5 ms width, and a 0.5 ms trailing edge were used. (c) Controlling the optical phase inside the racetrack. For RESET, pulses of 5.3, 5.4, and 5.6 V were used with a 400 ns width and 8 ns trailing edge. For SET, a pulse of 2.7 V, a 1.5 ms width, and a 0.5 ms trailing edge were used. (d) Tuning the coupling without changing the resonance wavelength via phase compensation. The pulse conditions are listed in Table S2 of the SI.

cross and bar states. We then fabricated these identified designs for electrical control. The 33-μm-long Sb_2Se_3 on the waveguide is electrically controlled by an integrated silicon PIN diode microheater.[17] The optical micrograph and scanning electron micrograph (SEM) images of a fabricated device before Al_2O_3 encapsulation are shown in Figure 2a. The SEM shows good alignment of the deposited Sb_2Se_3 with the Si waveguide. Figure 2b shows repeatable switching of light between the cross and bar ports for two consecutive cycles, which corresponds to the states shown in the schematics in Figure 2c. We measured broadband nonvolatile switching of light over a 50 nm bandwidth near the telecommunication C band (detail of the experimental setup is described in the Methods). The extinction ratio is ∼8 dB in the cross state and ∼15 dB in the bar state near 1530 nm. The insertion loss from the measured transmission is ∼1 dB in the cross state and ∼0.5 dB in the bar state near 1530 nm. However, the actual insertion loss is only ∼0.36 dB if deviation from the optimal coupling condition is considered, as we have discussed in section S4 of the SI. The loss caused by doping is negligible as the waveguide remains undoped and has been well studied in our previous paper.[17] For more details on the design and heat transfer simulation of the PIN diode heaters, we refer the readers to our previous works on the modeling[19] and experimental demonstration[11,17] of PIN diode heaters for controlling PCMs, since the heater geometry and doping used in this work are exactly the same as our previous works. Additionally, there are also numerous works from other groups around the world which have used either PIN or doped Si heaters to switch PCMs.[9,20−22]

Once we can electrically control the waveguide coupling using Sb_2Se_3, it also becomes possible to individually control the coupling and the phase in a racetrack resonator. Such a task has been proved extremely challenging for the traditional

https://doi.org/10.1021/acs.nanolett.3c03353
Nano Lett. XXXX, XXX, XXX−XXX

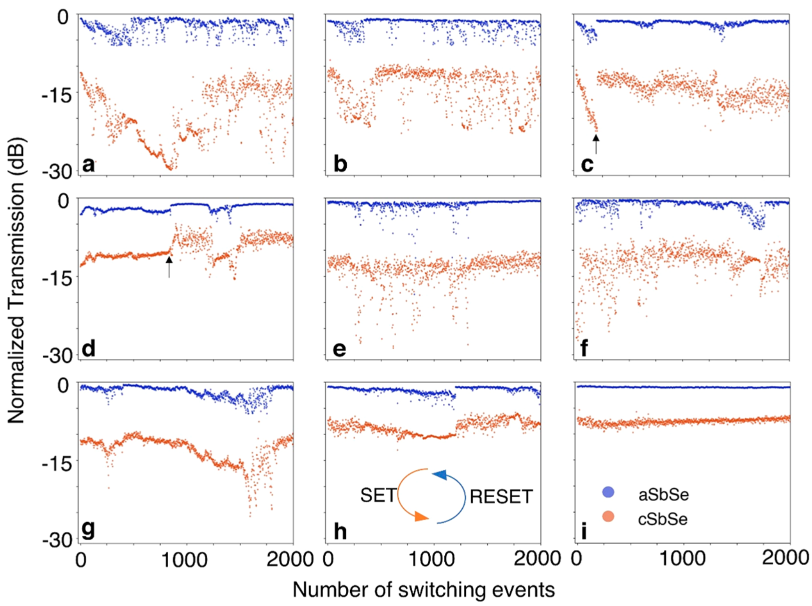

Figure 4. Endurance tests of the photonic switches. Endurance test of nine directional coupler switches measured at the cross port. For SET, 1.5-ms-wide, 0.5 ms trailing edge pulses are used. For RESET, 400-ns-wide, 8 ns trailing edge pulses are used. The pulse amplitudes are varied to prevent oversetting or resetting and are listed below for the corresponding cycles (SET/RESET): (a) 2.7/7.5 V (0 to 400); 2.7/7.6 V (401 to 1000). (b) 2.7/7.5 V (0 to 400); 2.7/7.6 V (401 to 700); 2.7/7.8 V (701 to 1000). (c) 2.6/7 V (0 to 100); 2.6/7.2 V (101 to 700); 2.6/7.3 V (701 to 1000). (d) 4/11 V (0 to 625); 4.2/11 V (626 to 1000). (e) 2.7/7.6 V (0 to 1000). (f) 2.8/7.5 V (0 to 200); 2.8/7.6 V (201 to 900); 2.8/7.7 V (901 to 1000). (g) 2.5/7.5 V (0 to 800); 2.5/7.6 V (801 to 1000). (h) 2.6/7 V (0 to 600); 2.6/7.1 V (601 to 1000). (i) 2.5/7.5 V (0 to 1000).

thermo-optic phase shifters due to thermal crosstalk, and they are also power-hungry.[15,16] In contrast, it can be realized readily using PCMs because the tuning is highly localized and nonvolatile. Figure 3a shows the device schematic (top) and an optical micrograph of the fabricated device (bottom). We can individually control the coupling between the racetrack and the bus waveguide, and the phase inside the racetrack, depending on the terminals (G1 or G2) that connect to the ground. Figure 3b shows the fully reversible and complete control of the coupling region from an initial undercoupling state (no resonance) to a critical coupling state (30 dB extinction ratio). The schematic on top shows the terminal that is grounded and the initial state of the device with spectra plotted in the first row. Note that as the extinction ratio is changed, the resonance wavelength also blue shifts as the optical phase inside the racetrack also depends on the coupling strength. This will be undesirable in applications such as trimming where the coupling of a microring should ideally be tuned at a fixed resonance wavelength. By changing the ground to G2, we can control the phase inside the racetrack without significantly changing the extinction ratio of the resonance (Figure 3c). Thus, by simultaneously controlling the coupling and the phase, we can compensate for the unwanted phase from changing the coupling, as shown in Figure 3d. After phase compensation, the coupling can be tuned to multiple levels without changing the resonance wavelength. Here, we achieved five different ERs (0, 13.4, 18.8, 28.5, and 34 dB) at the resonance wavelength of 1549.30 ± 0.01 nm. We discuss in detail how the phase compensation is performed and list all of the pulse conditions in section S9 of the SI.

Finally, we show excellent endurance of the switches over 1000 cycles across multiple devices on the same chip, which is sufficient for infrequent programming of the PICs, such as trimming and optical routing. 36 devices have been tested on the chip, and all can be switched reversibly, demonstrating outstanding reproducibility of the fabrication. Nine devices were randomly selected for the endurance test, as shown in Figure 4. All devices can be switched for more than 1000 cycles at a >10 dB extinction ratio, without significant degradation in the device performance. Note that in some situations we need to adjust the pulse amplitude to prevent oversetting or resetting. For example, the crystalline transmission in Figure 4d suddenly becomes very stochastic around the 800th event, indicated by an arrow. Meanwhile, the amorphous state transmission increases by around 1 dB. By raising the SET amplitude by 0.2 V at the 1250th event, the stochasticity in the crystalline state is suppressed, before becoming random again at the 1500th event. We think that this is caused by over-resetting the PCMs, which erases completely the crystalline seeds in the PCM on which growth of the crystalline phase can take place. As a result, during the subsequent setting operation, crystallization must be initiated through a nucleation process that introduces significant stochasticity. By raising the SET pulse amplitude to ensure complete crystallization, such randomness can be suppressed. On the other hand, it is also possible to overset. Figure 4c shows that the crystalline state transmission gradually decreases, while the amorphous transmission is very stochastic in the first 100 cycles (indicated by an arrow), a sign of oversetting. The oversetting could possibly be attributed to elemental segregation, which leads to regions in the PCM with an increased melting point. To remedy this issue, the reset pulse amplitude is raised by 0.2 V and the amorphous state becomes more deterministic.

The results presented here show that the switching conditions need to be optimized to minimize the stochasticity in both states. The pulse conditions may also need to be reoptimized to bring the switching back to a more deterministic state when the over-resetting/oversetting events occur. A potential solution is to implement an optimization script to automatically find the optimal pulse condition by

https://doi.org/10.1021/acs.nanolett.3c03353
Nano Lett. XXXX, XXX, XXX−XXX

minimizing the L_2 norm of the difference between the target state and the current state. In practice, the devices do not have to be switched constantly (once every few hours), so once the optimal conditions are found, the device can operate for a long time. Figure 4i shows that very deterministic switching over 1000 cycles is feasible once the optimal SET/RESET conditions are identified and no change in the pulse conditions is required.

To summarize, we demonstrated arbitrary programming of a racetrack resonator where the extinction ratio can be tuned without changing the resonance wavelength via independent control of the coupling and phase. Control of the coupling is achieved by a nonvolatile ultracompact directional coupler switch based on the low-loss PCM Sb_2Se_3. The directional coupler has a coupling length of only 33 μm and a broad operating wavelength range of over 50 nm. The extinction ratios are ∼15 dB/∼8 dB (bar/cross states), and the loss is as low as ∼0.36 dB near 1530 nm. Finally, nine devices were randomly selected for endurance testing, and all of them can be cycled 1000 times with a >10 dB extinction ratio, showing excellent fabrication reproducibility. This project paves the way to next-generation energy-efficient and compact programmable PICs. We believe the asymmetric optical response in the cross and bar states is due to the unoptimized phase matching conditions that lead to incomplete coupling of light to the cross port, which can be addressed with more extensive design of experiments in the future (see section S8 in the SI). Continuous control can also be implemented in the future to automatically perform the phase compensation when trimming the resonators or search for the optimal switching conditions during cycling. We think two major challenges for scaling to large systems are the insertion loss and uniformity. Consider a 16 × 16 switch array based on traditional MZI switches, where each optical path traverses seven stages of switching elements;[23] the total insertion loss from the switches alone is ∼6.7 dB. By replacing the MZIs with our design, the insertion loss can be reduced to 7 × 0.36 dB = 2.52 dB, thanks to the elimination of fourteen 2 × 2 couplers required for 50:50 power splitting in MZIs. The insertion loss of 0.36 dB can be further reduced by tapering the PCM film[9] and subwavelength PCM segments,[21] to mitigate the reflection and scattering loss, respectively. Additionally, the higher bend loss of rib waveguides can be reduced by using euler S-bends.[24] At the system level, uniformity also becomes an important consideration, which is the variation of the device performance (e.g., insertion loss, crosstalk, etc.) across the entire wafer. Even one switch with a poor performance can render the entire system useless. To reduce die-to-die or even device-to-device variation, foundries can optimize their fabrication processes to allow a smaller standard deviation in key design parameters such as waveguide widths, etch depths, and Si thickness. On the other hand, one can also adopt more fabrication-tolerant designs such as a diabatic or bent directional couplers[25−27] to replace the traditional straight couplers.

A few important implications of the demonstrated capability of independently controlled coupling rate and phase-shift in a ring resonator include the following: (1) An arbitrarily programmable racetrack resonator can find applications in photonic neural networks as tunable weights. For example, a typical wavelength-parallel photonic tensor core based on microring crossbar arrays[28,29] will require precise control of the rings' resonance wavelength—to align with the laser wavelength—and the extinction ratio—to adjust the weight. (2) Microring modulators are popular candidates to be used in the next-generation photonic transceivers due to their compact size and the intrinsic advantage of implementing wavelength-division-multiplexing with wavelength tuning by different ring radii or integrated heaters.[30] By introducing a nonvolatile programming element into the modulators, we can precisely align the resonance wavelength with the laser wavelength while maximizing the modulation depth without consuming any static power. (3) Microrings are also widely used as the resonators for integrated photonic lasers—commonly found in photonic transceivers and LiDAR systems—which consist of two or even four rings to form mirrors.[31] The coupling rate and the resonance wavelength of both rings have to be carefully tuned to align the resonance wavelengths of the two rings and minimize the linewidth. As more rings are used, the thermal crosstalk and the power consumption of the heaters will be more severe, whereas a nonvolatile component will be ideal for this task.

METHODS

Device Fabrication. The fabrication process mainly follows our previous works.[11,17] The silicon photonic devices were fabricated on a commercial SOI wafer with 220-nm-thick silicon on 2-μm-thick SiO_2 (WaferPro). All devices were defined using electron-beam lithography (EBL, JEOL JBX-6300FS) with a positive-tone electron beam resist (ZEP-520A) and partially etched by ∼120 nm in a fluorine-based inductively coupled plasma etcher (ICP, Oxford PlasmaLab 100 ICP-18) with mixed SF_6/C_4F_8. The doping regions were defined by two additional EBL rounds with 600-nm-thick poly(methyl methacrylate) (PMMA) resist and implanted by boron (phosphorus) ions for p++ (n++) doping regions with a dose of 2×10^{15} ions per cm^2 and ion energy of 14 keV (40 keV). The chips were annealed at 950 °C for 10 min (Expertech CRT200 Anneal Furnace) for dopant activation. Ohmic contact was formed after removal of the surface native oxide via immersing the chips in 10:1 buffered oxide etchant (BOE) for 10 s. The metal contacts were then immediately patterned by a fourth EBL step using PMMA. Metallization was done by electron beam evaporation (CHA SEC-600) and lift-off of Ti/Pd (5 nm/180 nm). After a fifth EBL defining the Sb_2Se_3 window, a 20 nm Sb_2Se_3 thin film was deposited via thermal evaporation from Sb_2Se_3 at a base pressure of 2×10^{-6} Torr, followed by a lift-off process. The chips were then annealed at 200 °C in an Ar atmosphere for 10 min to crystallize the Sb_2Se_3. The Sb_2Se_3 was then encapsulated by 40-nm-thick Al_2O_3 through thermal atomic layer deposition (Cambridge Nanotech Savannah 200) at 150 °C. To ensure good contact between the electric probe and metal pads while applying electrical pulses, the Al_2O_3 on the metal contacts was removed by defining a window using a sixth EBL with 600 nm PMMA, then etching in a chlorine-based inductively coupled plasma etcher (ICPRIE, Oxford PlasmaLab 100 ICP-18).

Electro-Optical Testing. The programmable units were measured with a 25°-angled vertical fiber-coupling setup. The stage temperature was controlled at 25 °C by a thermoelectric controller (TEC, TE Technology TC-720). A tunable continuous-wave laser (Santec TSL-510) was sent into the input light, the polarization of which was controlled by a manual fiber polarization controller (Thorlabs FPC526) to achieve a maximum fiber-to-chip coupling efficiency. A low-noise-power meter (Keysight 81634B) measured the static optical transmission. The transmission spectra were normal-

https://doi.org/10.1021/acs.nanolett.3c03353
Nano Lett. XXXX, XXX, XXX−XXX

ized to the spectra of the nearest reference waveguide. For the on-chip electrical switching, electrical pulses were applied to the on-chip metal contacts via a pair of electrical probes on two probe positioners (Cascade Microtech DPP105-M-AI-S). The crystallization and amorphization pulses were generated from a pulse function generator (Keysight 81160A). The tunable laser, power meter, thermal controller, source meter, and pulse function arbitrary generator were controlled by a LabView program. Note that a vertical fiber coupling setup was used for testing[11,32] with two fiber tips pointing toward each other. The noise in Figure 2b is caused by light from one fiber reflecting off the chip surface and collected by the other fiber across the device. To reduce the reflection, the input and output grating couplers can be offset by a larger distance in y (x−y defines the chip surface, where z is the normal). Due to constraints of the chip size and the need to put as many devices on the same chip as possible, such an offset was unfortunately not designed to be large enough to suppress the reflection. Alternatively, one can also use a fiber array and design the input and output grating couplers to be on the same side.

■ ASSOCIATED CONTENT

Supporting Information

The Supporting Information is available free of charge at https://pubs.acs.org/doi/10.1021/acs.nanolett.3c03353.

> Design of the directional coupler switch, simulation of the waveguide bend and reflection loss, simulation of lower port injection into the Sb_2Se_3 loaded waveguide, insertion loss of the photonic switches, SEM of an as-deposited and as-switched device, experimental refractive index change of Sb_2Se_3, simulated transmission with experimentally measured cSb_2Se_3 loss, optimizing the phase matching conditions via parameter sweep, arbitrary trimming of a racetrack resonator, performance comparison to other PCM-based photonic switches, further discussion on switching speed, switching energies, refractive index from ellipsometry and cutback measurements, discussion on the use of a racetrack resonator (PDF)

■ AUTHOR INFORMATION

Corresponding Authors

Juejun Hu − *Department of Materials Science and Engineering, Massachusetts Institute of Technology, Cambridge, Massachusetts 02139, United States;* orcid.org/0000-0002-7233-3918; Email: hujuejun@mit.edu

Arka Majumdar − *Department of Electrical and Computer Engineering, University of Washington, Seattle, Washington 98195, United States; Department of Physics, University of Washington, Seattle, Washington 98195, United States;* orcid.org/0000-0003-0917-590X; Email: arka@uw.edu

Authors

Zhuoran Fang − *Department of Electrical and Computer Engineering, University of Washington, Seattle, Washington 98195, United States;* orcid.org/0000-0001-8724-6633

Brian Mills − *Department of Materials Science and Engineering, Massachusetts Institute of Technology, Cambridge, Massachusetts 02139, United States*

Rui Chen − *Department of Electrical and Computer Engineering, University of Washington, Seattle, Washington 98195, United States;* orcid.org/0000-0001-8492-729X

Jieying Zhang − *Faculty of Electrical Engineering and Computer Science, Ningbo University, Ningbo 315211, China; Key Laboratory of Photoelectric Detection Materials and Devices of Zhejiang Province, Ningbo 315211, China*

Peipeng Xu − *Faculty of Electrical Engineering and Computer Science, Ningbo University, Ningbo 315211, China; Key Laboratory of Photoelectric Detection Materials and Devices of Zhejiang Province, Ningbo 315211, China*

Complete contact information is available at: https://pubs.acs.org/10.1021/acs.nanolett.3c03353

Author Contributions

[#]Z.F. and B.M. contributed equally to this work. Z.F. and A.M. conceived the project. Z.F. designed the photonic devices, performed electro-optical testing, and analyzed the data. B.M. deposited and patterned the Sb_2Se_3 for the electrically controlled photonic switches. R.C. fabricated the electrically controlled photonic switches and measured the passive photonic devices used in the parameter sweep. J.Z. and P.X. deposited the Sb_2Se_3 for the passive photonic devices used in the parameter sweep. A.M. and J.H. supervised the project. Z.F. wrote the manuscript with input from all authors. All authors have given approval to the publication of the manuscript.

Funding

The research is funded by NSF-2003509, ONR-YIP Award, DARPA-YFA Award, NASA-STTR Award 80NSSC22PA980, the National Key Research and Development Program of China (2021YFB2801300), and Intel.

Notes

The authors declare no competing financial interest.

■ ACKNOWLEDGMENTS

The authors acknowledge the fabrication facility supported by the Washington Nanofabrication Facility/Molecular Analysis Facility, a National Nanotechnology Coordinated Infrastructure (NNCI) site at the University of Washington, with partial support from the National Science Foundation via awards NNCI-1542101 and NNCI-2025489.

■ REFERENCES

(1) Cheng, Q.; Rumley, S.; Bahadori, M.; Bergman, K. Photonic Switching in High Performance Datacenters [Invited]. *Opt. Express, OE* **2018**, *26* (12), 16022−16043.

(2) Shen, Y.; Harris, N. C.; Skirlo, S.; Prabhu, M.; Baehr-Jones, T.; Hochberg, M.; Sun, X.; Zhao, S.; Larochelle, H.; Englund, D.; Soljačić, M. Deep Learning with Coherent Nanophotonic Circuits. *Nature Photon* **2017**, *11* (7), 441−446.

(3) Arrazola, J. M.; Bergholm, V.; Brádler, K.; Bromley, T. R.; Collins, M. J.; Dhand, I.; Fumagalli, A.; Gerrits, T.; Goussev, A.; Helt, L. G.; Hundal, J.; Isacsson, T.; Israel, R. B.; Izaac, J.; Jahangiri, S.; Janik, R.; Killoran, N.; Kumar, S. P.; Lavoie, J.; Lita, A. E.; Mahler, D. H.; Menotti, M.; Morrison, B.; Nam, S. W.; Neuhaus, L.; Qi, H. Y.; Quesada, N.; Repingon, A.; Sabapathy, K. K.; Schuld, M.; Su, D.; Swinarton, J.; Száva, A.; Tan, K.; Tan, P.; Vaidya, V. D.; Vernon, Z.; Zabaneh, Z.; Zhang, Y. Quantum Circuits with Many Photons on a Programmable Nanophotonic Chip. *Nature* **2021**, *591* (7848), 54−60.

(4) Watts, M. R.; Sun, J.; DeRose, C.; Trotter, D. C.; Young, R. W.; Nielson, G. N. Adiabatic Thermo-Optic Mach-Zehnder Switch. *Opt. Lett., OL* **2013**, *38* (5), 733−735.

(5) Errando-Herranz, C.; Takabayashi, A. Y.; Edinger, P.; Sattari, H.; Gylfason, K. B.; Quack, N. MEMS for Photonic Integrated Circuits. *IEEE J. Sel. Top. Quantum Electron.* **2020**, *26* (2), 1−16.

(6) Fang, Z.; Chen, R.; Zheng, J.; Majumdar, A. Non-Volatile Reconfigurable Silicon Photonics Based on Phase-Change Materials. *IEEE J. Sel. Top. Quantum Electron.* **2022**, *28*, 1−1.

(7) Fang, Z.; Chen, R.; Zheng, J.; Khan, A. I.; Neilson, K. M.; Geiger, S. J.; Callahan, D. M.; Moebius, M. G.; Saxena, A.; Chen, M. E.; Rios, C.; Hu, J.; Pop, E.; Majumdar, A. Ultra-Low-Energy Programmable Non-Volatile Silicon Photonics Based on Phase-Change Materials with Graphene Heaters. *Nat. Nanotechnol.* **2022**, 1−7.

(8) Delaney, M.; Zeimpekis, I.; Du, H.; Yan, X.; Banakar, M.; Thomson, D. J.; Hewak, D. W.; Muskens, O. L. Nonvolatile Programmable Silicon Photonics Using an Ultralow-Loss Sb2Se3 Phase Change Material. *Science Advances* **2021**, *7* (25), eabg3500.

(9) Ríos, C.; Du, Q.; Zhang, Y.; Popescu, C.-C.; Shalaginov, M. Y.; Miller, P.; Roberts, C.; Kang, M.; Richardson, K. A.; Gu, T.; Vitale, S. A.; Hu, J. Ultra-Compact Nonvolatile Phase Shifter Based on Electrically Reprogrammable Transparent Phase Change Materials. *PhotoniX* **2022**, *3* (1), 26.

(10) Fang, Z.; Zheng, J.; Saxena, A.; Whitehead, J.; Chen, Y.; Majumdar, A. Non-Volatile Reconfigurable Integrated Photonics Enabled by Broadband Low-Loss Phase Change Material. *Advanced Optical Materials* **2021**, *9* (9), 2002049.

(11) Chen, R.; Fang, Z.; Fröch, J. E.; Xu, P.; Zheng, J.; Majumdar, A. Broadband Nonvolatile Electrically Controlled Programmable Units in Silicon Photonics. *ACS Photonics* **2022**, *9* (6), 2142−2150.

(12) Chen, R.; Fang, Z.; Perez, C.; Miller, F.; Kumari, K.; Saxena, A.; Zheng, J.; Geiger, S. J.; Goodson, K. E.; Majumdar, A. Non-Volatile Electrically Programmable Integrated Photonics with a 5-Bit Operation. *Nat. Commun.* **2023**, *14* (1), 3465.

(13) Xu, P.; Zheng, J.; Doylend, J. K.; Majumdar, A. Low-Loss and Broadband Nonvolatile Phase-Change Directional Coupler Switches. *ACS Photonics* **2019**, *6* (2), 553−557.

(14) Zhang, Q.; Zhang, Y.; Li, J.; Soref, R.; Gu, T.; Hu, J. Broadband Nonvolatile Photonic Switching Based on Optical Phase Change Materials: Beyond the Classical Figure-of-Merit. *Opt. Lett., OL* **2018**, *43* (1), 94−97.

(15) Milanizadeh, M.; Aguiar, D.; Melloni, A.; Morichetti, F. Canceling Thermal Cross-Talk Effects in Photonic Integrated Circuits. *Journal of Lightwave Technology* **2019**, *37* (4), 1325−1332.

(16) Miller, S. A.; Okawachi, Y.; Ramelow, S.; Luke, K.; Dutt, A.; Farsi, A.; Gaeta, A. L.; Lipson, M. Tunable Frequency Combs Based on Dual Microring Resonators. *Opt. Express, OE* **2015**, *23* (16), 21527−21540.

(17) Zheng, J.; Fang, Z.; Wu, C.; Zhu, S.; Xu, P.; Doylend, J. K.; Deshmukh, S.; Pop, E.; Dunham, S.; Li, M.; Majumdar, A. Nonvolatile Electrically Reconfigurable Integrated Photonic Switch Enabled by a Silicon PIN Diode Heater. *Adv. Mater.* **2020**, *32* (31), 2001218.

(18) Teo, T. Y.; Krbal, M.; Mistrik, J.; Prikryl, J.; Lu, L.; Simpson, R. E. Comparison and Analysis of Phase Change Materials-Based Reconfigurable Silicon Photonic Directional Couplers. *Opt. Mater. Express, OME* **2022**, *12* (2), 606−621.

(19) Zheng, J.; Zhu, S.; Xu, P.; Dunham, S.; Majumdar, A. Modeling Electrical Switching of Nonvolatile Phase-Change Integrated Nanophotonic Structures with Graphene Heaters. *ACS Appl. Mater. Interfaces* **2020**, *12* (19), 21827−21836.

(20) Zhang, H.; Zhou, L.; Lu, L.; Xu, J.; Wang, N.; Hu, H.; Rahman, B. M. A.; Zhou, Z.; Chen, J. Miniature Multilevel Optical Memristive Switch Using Phase Change Material. *ACS Photonics* **2019**, *6* (9), 2205−2212.

(21) Yang, X.; Lu, L.; Li, Y.; Wu, Y.; Li, Z.; Chen, J.; Zhou, L. Non-Volatile Optical Switch Element Enabled by Low-Loss Phase Change Material. *Adv. Funct. Mater.* **2023**, *33* (42), 2304601.

(22) Zhou, W.; Dong, B.; Farmakidis, N.; Li, X.; Youngblood, N.; Huang, K.; He, Y.; David Wright, C.; Pernice, W. H. P.; Bhaskaran, H. In-Memory Photonic Dot-Product Engine with Electrically Programmable Weight Banks. *Nat. Commun.* **2023**, *14* (1), 2887.

(23) Lu, L.; Zhao, S.; Zhou, L.; Li, D.; Li, Z.; Wang, M.; Li, X.; Chen, J. 16 × 16 Non-Blocking Silicon Optical Switch Based on Electro-Optic Mach-Zehnder Interferometers. *Opt. Express, OE* **2016**, *24* (9), 9295−9307.

(24) Bahadori, M.; Nikdast, M.; Cheng, Q.; Bergman, K. Universal Design of Waveguide Bends in Silicon-on-Insulator Photonics Platform. *Journal of Lightwave Technology* **2019**, *37* (13), 3044−3054.

(25) Chen, S.; Shi, Y.; He, S.; Dai, D. Low-Loss and Broadband 2 × 2 Silicon Thermo-Optic Mach-Zehnder Switch with Bent Directional Couplers. *Opt. Lett., OL* **2016**, *41* (4), 836−839.

(26) Ding, Y.; Liu, L.; Peucheret, C.; Ou, H. Fabrication Tolerant Polarization Splitter and Rotator Based on a Tapered Directional Coupler. *Opt. Express, OE* **2012**, *20* (18), 20021−20027.

(27) Luo, Y.; Yu, Y.; Ye, M.; Sun, C.; Zhang, X. Integrated Dual-Mode 3 dB Power Coupler Based on Tapered Directional Coupler. *Sci. Rep* **2016**, *6* (1), 23516.

(28) Huang, C.; Bilodeau, S.; Ferreira de Lima, T.; Tait, A. N.; Ma, P. Y.; Blow, E. C.; Jha, A.; Peng, H.-T.; Shastri, B. J.; Prucnal, P. R. Demonstration of Scalable Microring Weight Bank Control for Large-Scale Photonic Integrated Circuits. *APL Photonics* **2020**, *5* (4), 040803.

(29) Xiao, X.; Cheung, S.; Hooten, S.; Peng, Y.; Tossoun, B.; Vaerenbergh, T. V.; Kurczveil, G.; Beausoleil, R. G.Wavelength-Parallel Photonic Tensor Core Based on Multi-FSR Microring Resonator Crossbar Array. In *Optical Fiber Communication Conference (OFC) 2023 (2023)*; paper W3G.4; Optica Publishing Group, 2023; p W3G.4. DOI: 10.1364/OFC.2023.W3G.4.

(30) Levy, C.; Xuan, Z.; Huang, D.; Kumar, R.; Sharma, J.; Kim, T.; Ma, C.; Su, G.-L.; Liu, S.; Kim, J.; Wu, X.; Balamurugan, G.; Rong, H.; Jaussi, J. A 3D-Integrated 8λ × 32 Gbps λ Silicon Photonic Microring-Based DWDM Transmitter. In *2023 IEEE Custom Integrated Circuits Conference (CICC)*; IEEE, 2023; pp 1−2. DOI: 10.1109/CICC57935.2023.10121265.

(31) Tran, M. A.; Huang, D.; Bowers, J. E. Tutorial on Narrow Linewidth Tunable Semiconductor Lasers Using Si/III-V Heterogeneous Integration. *APL Photonics* **2019**, *4* (11), 111101.

(32) Zheng, J.; Fang, Z.; Wu, C.; Zhu, S.; Xu, P.; Doylend, J. K.; Deshmukh, S.; Pop, E.; Dunham, S.; Li, M.; Majumdar, A. Nonvolatile Electrically Reconfigurable Integrated Photonic Switch Enabled by a Silicon PIN Diode Heater. *Adv. Mater.* **2020**, *32* (31), 2001218.

https://doi.org/10.1021/acs.nanolett.3c03353
Nano Lett. XXXX, XXX, XXX−XXX